

# Computational simulation of a magnetic microactuator for tissue engineering applications

Joseph Keyes · Michael Junkin · Pak Kin Wong · Jonathan P. Vande Geest

© Springer Science + Business Media, LLC 2009

**Abstract** The next generation of tissue engineered constructs (TECs) requires the incorporation of a controllable and optimized microstructure if they are to chemically, mechanically, and biologically mimic tissue function. In order to obtain TECs with optimized microstructures, a combination of spatiotemporally regulated mechanical and biochemical stimuli is necessary during the formation of the construct. While numerous efforts have been made to create functional tissue constructs, there are few techniques available to stimulate TECs in a localized manner. We herein describe the design of a microdevice which can stimulate TECs in a localized, inhomogeneous, and predefined anisotropic fashion using ferromagnetically doped polydimethylsiloxane microflaps (MFs). Specifically, a sequential magneto-structural finite element model of the proposed microdevice is constructed and utilized to understand how changes in magnetic and geometrical properties of the device affect MF deflection. Our study indicates that a relatively small density of ferromagnetic material is required to result in adequate force and MF deflection ( $175\ \mu\text{m}$   $\sim$ 7% TEC strain). We also demonstrate

that MF to magnet distance is more important than inherent MF magnetic permeability in determining resulting MF deflection. An experimental validation test setup was used to validate the computational solutions. The comparison shows reasonable agreement indicating a 5.9% difference between experimentally measured and computationally predicted MF displacement. Correspondingly, an apparatus with two MFs and two magnets has been made and is currently undergoing construct testing. The current study presents the design of a novel magnetic microactuator for tissue engineering applications. The computational results reported here will form the foundation in the design and optimization of a functional microdevice with multiple MFs and magnets capable of stimulating TECs in nonhomogenous and preferred directions with relevant spatial resolution.

**Keywords** Tissue engineering · Biomechanics · Magnetic · Microactuator · Finite element

## 1 Introduction

The 3D microstructure of tissue-engineered constructs (TECs) and their resulting mechanical and biological properties are critical in providing TECs with clinically meaningful functionality. We hypothesize that the next generation of TECs should incorporate a controllable and optimized microstructure (and resulting mechanical properties) if they are to chemically, mechanically, and biologically mimic tissue function. Mechanical stimulation of cell-gel constructs represents a promising candidate for manipulating the environmental (matrix), biochemical, and mechanical properties of TECs (Eastwood et al. 1998; Kanda & Matsuda 1994; Seliktar et al. 2000). Bulk mechanical stimulation approaches have proven to be

---

M. Junkin · P. K. Wong · J. P. Vande Geest (✉)  
Aerospace and Mechanical Engineering,  
The University of Arizona,  
1130 N Mountain Ave, PO Box 210119,  
Tucson, AZ 85721-0119, USA  
e-mail: jpv1@email.arizona.edu

J. Keyes · P. K. Wong · J. P. Vande Geest  
Graduate Interdisciplinary Program in Biomedical Engineering,  
The University of Arizona,  
Tucson, AZ, USA

P. K. Wong · J. P. Vande Geest  
BIO5 Institute for Biocollaborative Research,  
The University of Arizona,  
Tucson, AZ, USA

advantageous in improving the mechanical strength of TECs (Liao et al. 2004; Wnek et al. 2008); however, the development of a TEC with well defined local microstructures, which are often observed in their natural counterparts, cannot be achieved using such bulk stimulation methods (L'Heureux et al. 1998). Because the overall functionality of tissues is affected by local stimuli (McKee et al. 2003; Niklason et al. 1999), the ability to control these stimuli at the micro-scale will provide new and exciting opportunities in tissue engineering. A device capable of imposing localized micro-mechanical stimulation is highly desirable and will open the possibility of creating TECs with controllable local microstructures.

The advent of microelectromechanical systems (MEMS) provides new opportunities to manipulate the microenvironment of cells and matrices. The proper length scale matching of MEMS and cells will enable localized stimulation and sensing of TECs with unprecedented resolution (Kim et al. 2009). For instance, previous studies have applied microfabricated magnetic microposts to measure the forces created by cells and to apply external forces to cells (Armani 1999; Miller 2001; Tan et al. 2003). These studies indicate the feasibility of using these magnetic-field-susceptible MEMS devices for manipulating cellular-sized systems by using several different methods. These methods have focused on microfluidic and single cell manipulation applications and not on the stimulation of groups of cells within a TEC (Khoo & Liu 2001; Kretschmer et al. 2002; Sadler et al. 1998). Since the performance of the magnetic microactuator is governed by several interrelated mechanical, geometrical and magnetic design parameters, a detailed investigation will be beneficial for the design of the magnetic microdevices and will pave the way for creating TECs with controllable microstructures.

In this paper the concept of a MEMS-based device that can differentially stimulate the mechanical microenvironment of TECs using a noninvasive magnetic actuation

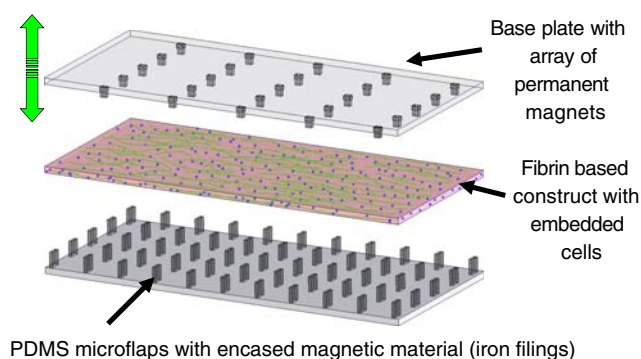


**Fig. 1** Concept for a MEMS-based micro-stimulation of tissue engineered constructs. Concept of array of micro-flaps showing stackup of micro-flap bed, magnet array, and tissue-engineering construct

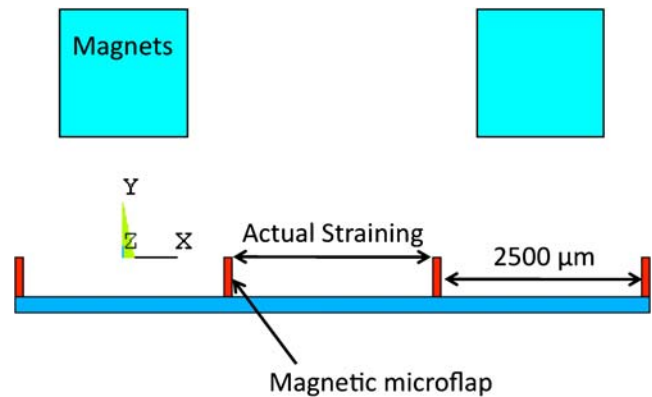


**Fig. 2** Concept of the fixture to provide strain into the material placed atop the flap. The neodymium magnets are light blue, the PDMS without magnetic particles is blue, and the micro-flaps with magnetic particles are red

mechanism is introduced. The device consists of a bed of polymeric micro-flaps (MFs) doped with ferromagnetic particles. Translating an array of permanent magnets close to the TEC, which sits on the bed of MFs (Fig. 1), actuates these MFs and locally stimulates the TEC. The directionality of the MFs shown in Fig. 1 are uniaxial for simplicity. A system which stimulates the construct in localized, inhomogeneous, and predefined anisotropic strains can easily be obtained with appropriate design of the micro-fabrication process. Since fabricating large number of devices with different parameters can be time consuming and costly, the purpose of the current work is to develop a computational tool that can aid in the design of this MEMS-based actuator. A sequential magneto-structural finite element model of the device is constructed and utilized to understand how changes in the magnetic properties of the MFs and their relative distance to the permanent magnets affects MF horizontal displacement. The resulting information will provide useful insights and practical guidelines for the assembly of first generation MF devices which are useful for simulation of TECs.

## 2 Materials and methods

### 2.1 Computational simulation of microflaps

Figure 2 shows a diagram of the microdevice stretching concept, where the MFs are made of polydimethylsiloxane (PDMS) doped with iron filings. The TEC would either sit on the top of the bed of MFs or would be immersed within them. When the magnets (light blue, with coercive force vector applied in the vertical dimension) approach the four MFs (red), the MFs will displace laterally. Straining occurs between the two center MFs. This setup was simulated

using the commercially available magneto-structural finite element program ANSYS v. 10.

The mechanical properties of the PDMS in the computational model were taken from the literature (Armani 1999). Table 1 summarizes all of the material properties utilized in our computational study. We assumed the magnetic properties of the PDMS were close to other materials that do not exhibit high susceptibility to magnetic fields ( $\mu_r \approx 1$ ) (Sniadecki et al. 2007). This is a viable assumption as these materials do not alter an induced magnetic field. The manufacturer provided the permanent magnet's mechanical and magnetic properties (K&J Magnetics 2007). The doped PDMS (with iron filings) were assumed to have structural mechanical properties equal to that of the un-doped PDMS. The magnetic properties of the doped-PDMS were extrapolated as going down linearly with volume of iron filings in the PDMS. For example, adding a specific material with an initial permeability of 10 into a 1:1 mixture by volume of PDMS will result in a relative permeability of 5.5. To complete the magneto-structural analysis, magnetic forces must first be calculated in the magnetic physics environment to determine the forces acting on the flaps. These forces are exported to a structural model with the same elements. This means air elements are in the structural solving environment, and the program must include them in solving this stage of the analysis. This includes inputting values for Poisson's ratio and Young's modulus. For simplicity, the bulk modulus of air and a Poisson's ratio of 0.499 was used to determine a Young's modulus for air using (Gere 2004):

$$\kappa = \frac{E}{3(1-2\nu)} \quad (1)$$

Note that the value for  $E$  used here is an order of magnitude smaller than that used for the MFs (61 Pa versus 750 kPa, respectively). In Table 1, the structural components of the analysis were assumed to be homogenous and isotropic, while the magnetic materials were assumed to be in the unsaturated, linear portions of their respective B-H curves.

A 500  $\mu\text{m}$  high by 100  $\mu\text{m}$  thick arrangement of MFs with a separation of 2500  $\mu\text{m}$  provided the geometric baseline. A sensitivity study was performed on the following system parameters: magnet size, magnet-to-MF separation, and magnetic particle density within the PDMS. An optimal magnetic particle density for mixing was determined first, after which the geometry and location of small magnets were optimized to obtain a deflection at the top of the two central MFs in the x-direction of about 175  $\mu\text{m}$ . This value would correspond to 7% strain in the TEC. The density of the iron filings within the PDMS (permeability) was also optimized.

Magnetic and structural FEMs were solved sequentially using 8-node quadrilateral magnetic and structural elements for all materials. Infinite boundary elements were used around the air elements. The model had 8,568 nodes with a refinement ratio of 3.0 from the air edge to areas with high magnetic field density or deflection areas of interest around the MFs (Brown 1995).

Once the magnetic forces were obtained in the magnetic FEM, they were saved and exported to a structural analysis where they were used to cause MF deflection. The structural model was constrained at the top of the magnet, around the end boundaries of the air elements, and at the bottom of the un-doped PDMS in all degrees of freedom. The vertical portion of the un-doped PDMS was constrained only in the x-direction to simulate a symmetric effect.

Maxwell's equations were used to formulate the magnetic vector potentials in electromagnetic field analysis. All other results are derived from this vector formulation (Wang et al. 2003). The governing equations for the magnetic FEM are (ANSYS Inc 2006)

$$\nabla \times \{H\} = \{J\} \quad (2)$$

$$\nabla \times \{E\} = -\frac{\partial B}{\partial t} \quad (3)$$

$$\nabla \cdot \{B\} = 0 \quad (4)$$

where

- $\{H\}$  is the magnetic field intensity
- $\{J\}$  is the total current density
- $\{E\}$  is the electric field intensity, and
- $\{B\}$  is the magnetic flux density.

To obtain a solution for these equations, potentials were introduced expressed in Eqs. 5 and 6 (ANSYS Inc 2006).

$$\{B\} = \nabla \times \{A\} \quad (5)$$

$$\{E\} = -\left\{\frac{\partial A}{\partial t}\right\} - \nabla V \quad (6)$$

where

- $\{A\}$  is the magnetic vector potential
- $V$  is the electric scalar potential.

The constitutive relations describing the behavior of the magnetic materials were (Wang et al. 2003):

$$\{B\} = [\mu]\{H\} + \mu_0\{M_0\} \quad (7)$$

**Table 1** Mechanical properties used in the magneto-structural simulations

Material	Mechanical			Magnetic
	E (Pa)	$\nu$	$\mu_r$	$F_{\text{coersive}}$ (A/m)
PDMS (Liao et al. 2004)	750E3	0.49	1	N/A
Iron-Doped PDMS	750E3	0.49	Parameter	N/A
Air	60.6	0.499	1	N/A
Neodymium Magnet (Niklason et al. 1999)	1.67E11	0.17	1.058 (McKee et al. 2003)	875352 (in y)

where

- $\mu$  is the relative magnetic permeability matrix
- $\mu_0$  is the permeability of free space ( $4\pi \times 10^{-7}$  H/m)
- $\{M_0\}$  is the remnant intrinsic magnetization vector.

The relative permeability matrix for all materials used in the analysis (all materials assumed to be isotropic) is given by (ANSYS 2006)

$$[\mu] = \mu_0 \begin{bmatrix} \mu_{rx} & 0 & 0 \\ 0 & \mu_{ry} & 0 \\ 0 & 0 & \mu_{rz} \end{bmatrix} \quad (8)$$

where  $\mu_{rx}$  is the relative permeability in the x-direction.

The analysis assumed all materials to be isotropic, with the exception of the magnetic coersive force, which was input as being vertically magnetized. The constitutive relationship relating degrees of freedom, loads, and results as derived from Maxwell's equations for the plane-53 magnetic element (8-node quadrilateral element) is given by (ANSYS Inc 2006):

$$[\bar{C}]\{\dot{u}\} + [\bar{K}]\{\dot{u}\} = \{\bar{J}_i\} \quad (9)$$

where

- $[\bar{C}]$  and  $[\bar{K}]$  are coefficient matrices
- $\{\dot{u}\}$  is the degree of freedom vector
- $\{\bar{J}_i\}$  is the applied load vector.

Substituting all necessary terms into Eq. 9 and eliminating electrical components resulted in:

$$\begin{bmatrix} [K] & [0] \\ [0] & [0] \end{bmatrix} \begin{Bmatrix} \{A_e\} \\ \{0\} \end{Bmatrix} = \begin{Bmatrix} \{J^s\} + \{J^{pm}\} \\ \{0\} \end{Bmatrix} \quad (10)$$

where

- $[K]$  is the coefficient matrix taking into account the matrix element shape functions related to the material's properties,
- $\{A_e\}$  is the magnetic vector potential, and  $\{J^s\} + \{J^{pm}\}$  is the applied load vector that related the shape

functions to the coersive force from the permanent magnet.

Once the magnetic vector potential has been determined, the magnetic flux density is solved for using the following equation (ANSYS Inc 2006):

$$\{B\} = \nabla \times [N_A]^T \{A_e\} \quad (11)$$

where

$[N_A]$  are the shape functions.

The magnetic field intensity is then computed from the flux density

$$\{H\} = [v]\{B\} \quad (12)$$

where

$[v]$  is the reluctivity matrix (inverse of  $[\mu]$ ).

The MFs are then flagged as Maxwell surfaces and the resulting forces are output for solution of the structural problem. The program uses the results of Eq. 11 to determine these forces using the following equation.

$$\{F^{mx}\} = \frac{1}{\mu_0} \int_S \begin{bmatrix} T_{11} & T_{12} \\ T_{21} & T_{22} \end{bmatrix} \begin{Bmatrix} n_1 \\ n_2 \end{Bmatrix} dS \quad (13)$$

where

- $\{F^{mx}\}$  is the force acting on a region,
- $\begin{Bmatrix} n_1 \\ n_2 \end{Bmatrix}$  are unit normal vectors,
- and  $T_{ij}$  are the forces given by

$$T_{11} = B_x^2 - \frac{1}{2}|B|^2 \quad (14)$$

$$T_{12} = B_x B_y \quad (15)$$

$$T_{21} = B_x B_y \quad (16)$$

$$T_{22} = B_y^2 - \frac{1}{2}|B|^2 \quad (17)$$

Finally, these structural forces were exported to the structural physics environment to solve for deflection. Eight node quadrilateral structural elements were used to solve for MF displacement using the traditional theory of virtual work. The magnetic density and nodal displacement were results of interest, with polynomial interpolation used to generate contour plots. A key assumption other than those already discussed is that the model behaves under plane stress behavior (2D): This model assumes the width of a given MF to be relatively small, and the magnet's width will not be larger than the MF's width.

## 2.2 Experimental validation

To confirm that these simulations resulted in a meaningful MF deflection, a doped-PDMS flap was created with dimensions larger than the simulated MFs. A 1:10 ratio of catalyst to PDMS base was mixed by mass, then mixed with iron filings to a .119:1 by volume ratio, and finally vacuum pumped for degassing to create the doped-PDMS mixture. After the mixture cured on a microscope slide, the thickness of the PDMS was measured over the entire surface of the slide. The section that exhibited the smallest change in thickness ( $\pm 13 \mu\text{m}$ ) over an area of  $25 \text{ mm}^2$  was removed from the mold and cut with a razor blade to result in dimensions of 0.28 mm thick by 4.4 mm high by 2.4 mm wide. This was sandwiched between two microscope slides, turned on its side, and observed through a microscope. A 1/8" cube magnet at the tip of a ferrous set of tweezers and near the flap enabled displacement measurement by overlaying the system with a printed 300  $\mu\text{m}$  pattern. Figure 3 shows this setup. MF deflection was observed through a microscope when a 1/8" cube permanent magnet was brought to within 1.6 mm of the MF. This setup was

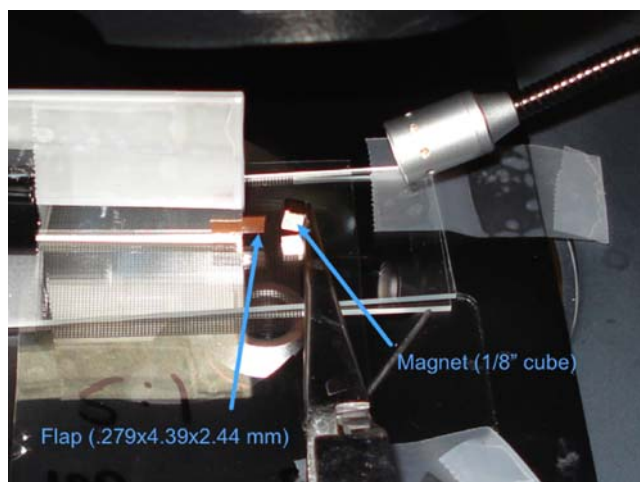


**Fig. 3** Physical setup for the scaled-up test shown on the microscope stand. The flap is brown on the left, with the cube magnet to the right

computationally created and solved using the simulation scheme described above for the four-MF analysis.

After these initial investigations a baseline design for cellular testing was constructed. An apparatus with a four-bar mechanism to allow a two-magnet array to move up and down sat above a MF mold with two MFs and a well. The system is entirely battery powered allowing it to sit in an incubator and cycle for 3 weeks based on calculations of power output from the motor (H02532-01D 71 rpm motor from hobbyengineering.com) and battery specifications (Carbon-Zinc batteries). Figure 4 shows the apparatus in an incubator.

## 3 Results

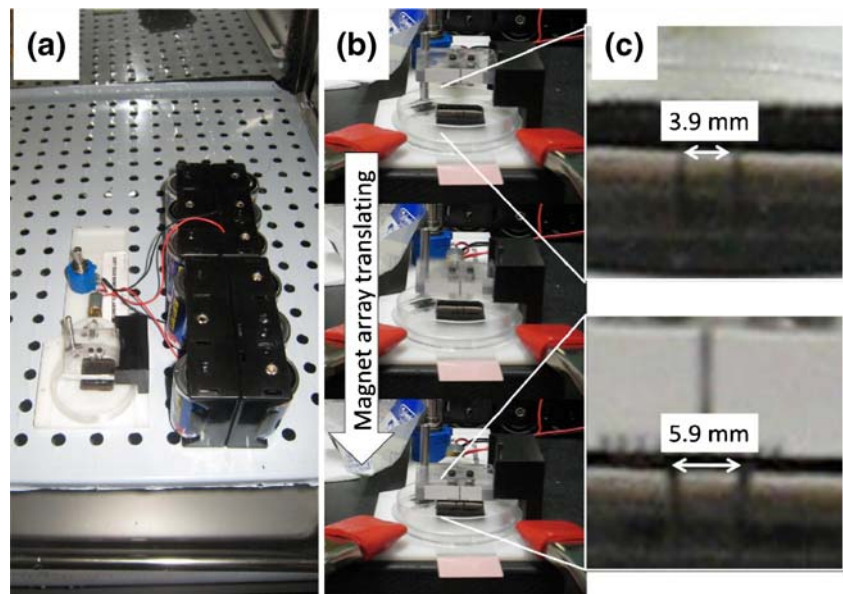
The first investigated parameter was the magnetic permeability of the PDMS MFs (related to the density of the particles of iron filings in the MF). Baseline models with the same dimensions as shown in Fig. 2 were used, however, with just one flap. The magnet was moved toward and away from the MF, and peak nodal forces were exported by using nine different models. Table 2 lists the individual differences in these models. Figure 5 graphically displays the results from Table 2. As one can see in this figure, MF displacement is more strongly dependent on MF-magnet distance than MF permeability. This result will allow us to use a minimum number of magnetic particles and focus more on a method for tight regulation of the magnet-flap separation. Figure 6 shows relationship between the force applied to the MF, the MF magnetic permeability, and the MF deflection. These results suggest that with a specific magnet to MF separation the applicable magnetic force on the MF will saturate at a specific magnetic permeability. This point actually occurs at relatively low permeabilities compared to the permeability of iron ( $\mu_{\text{iron}} = 5000$ ) (Askeland 2002). This means that with the expected location of the magnet in the final analysis, mixtures greater than  $\sim .119:1$  of iron filings to PDMS will not increase the force on the MF. As a result, low densities of iron filings may be used and the mechanical properties of the silicone can primarily be manipulated by varying the ratio of base to catalyst of the PDMS (Armani 1999).

Next, a model was developed with different magnet positions and four MFs. Four separate models were run with varying magnet size and magnet separation. An empirical exponential relationship was determined relating MF deflection and magnet separation (see Fig. 7).

$$U_x = 5.387e^{-1.763(\text{Separation})} \quad (18)$$

In order to isolate the appropriate magnet separation, the desired MF displacement was inserted and back-solved for

**Fig. 4** (a) Two microflap device within incubator (b) Translation of microflap device (c) Zoomed image of the two microflaps showing displacement from 3.9 mm to 5.9 mm



separation. This separation was 1.92 mm from the bottom of the magnet to the top of the MFs. A model was created with this separation and analyzed in depth.

Figure 8 shows a representative result of the magnetic computational analysis. The top of this figure displays the magnetic field lines, while the bottom illustrates the resulting magnetic vector lines. Note the modified magnetic field lines by the iron filings within the MFs. Figure 9 shows the force vector plot along with the contours of MF displacement resulting from the structural simulation. Placing the two magnets between the four microflaps results in the two center flaps moving away from one another and towards the magnets. The two central MFs experience less force than the outer MFs (and thus less displacement) since each of these is affected by the non-adjacent magnet (Fig. 9). As seen in

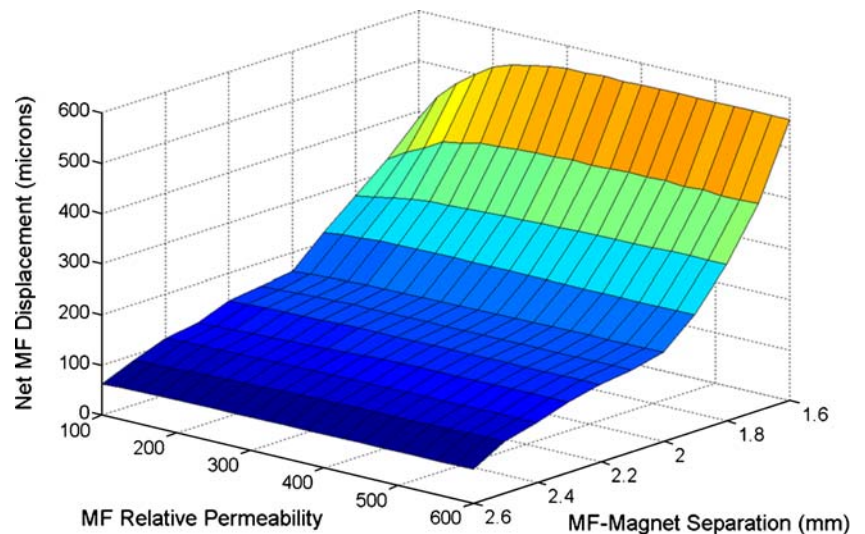
this figure, the displacement between the two central MFs was 180  $\mu\text{m}$ , which resulted in 7.2% strain between the tip of adjacent MFs.

The same computational scheme was applied to simulate the experimental validation setup. Figure 10 shows the analysis results at true deformation scale below the picture of the physical findings. The picture of the physical model shows the tip of the flap displaced in the upper-left-hand corner with a corner of the magnet at the upper-right-hand corner; shown transparent and outlined in red in the lower-left-hand corner is the flap's undeformed state. The error between the displacements of the two models was 5.9%. This can be attributed to three primary components: the resolution of the measurements through the microscope was 300  $\mu\text{m}$ , the flap was not exactly parallel to the optical axis

**Table 2** Details of parametric study

Baseline parameter values			
Magnet Size (mm square)	Magnet-MF Separation (mm)	MF Permeability	Displacement ( $\mu\text{m}$ )
0.57	2.6	100	12
Parametric Study			
Case Number	Changed Parameter	New Value	Displacement ( $\mu\text{m}$ )
1	Permeability	75	6
2	Permeability	40	6
3	Magnet Size (mm square)	1.59	78
	Permeability	595	
4	Magnet-MF Separation (mm)	2.53	64
5	Magnet-MF Separation (mm)	2	158
6	Magnet-MF Separation (mm)	1.5	76
7	Magnet-MF Separation (mm)	1.94	170
8	Magnet-MF Separation (mm)	1.92	185

**Fig. 5** Relationship between microflap displacement, permeability and MF-magnet separation



of the microscope leading to the image of the flap having a wider optical footprint, and the PDMS's properties were slightly modified due to the addition of the iron filings. This change, however, is likely to be rather small due to the low density of particles in the PDMS. The relatively small error between the scaled up physical experiment and its resulting computational simulation serves as a preliminary validation of the computational scheme.

**4 Discussion**

This study demonstrates that a magnetically actuated MEMS-based microdevice can be constructed and should allow for the differential and nonhomogenous stimulation

of tissue-engineered constructs. We demonstrate that MF to magnet distance is more important than inherent MF magnetic permeability in determining resulting MF deflection. An experimental validation test setup was used to validate the computational solutions. The current study presents the design of a novel magnetic microactuator for tissue engineering applications. The computational results reported here will form the foundation in the design and optimization of a functional microdevice with multiple MFs and magnets capable of stimulating TECs in nonhomogenous and preferred directions with relevant spatial resolution.

While other groups have investigated methods of manipulating cells using magnetic actuation, the application of MEMS magnetic microactuation for noninvasive TEC

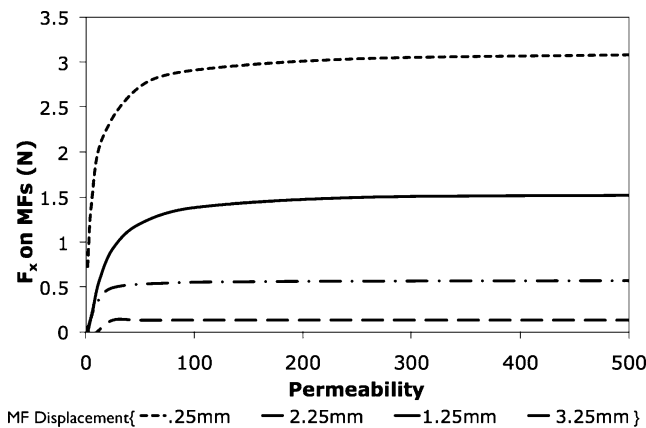


**Fig. 6** Relationship between microflap displacement and force as a function of different magnetic permeabilities

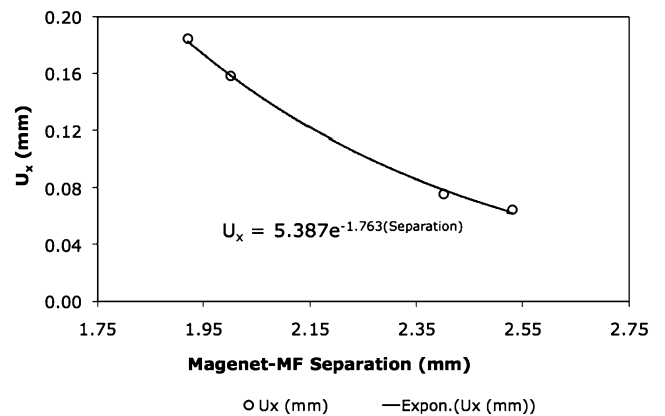


**Fig. 7** Results of the magnet to micro-flap separation's relation to Ux in the four micro-flap design

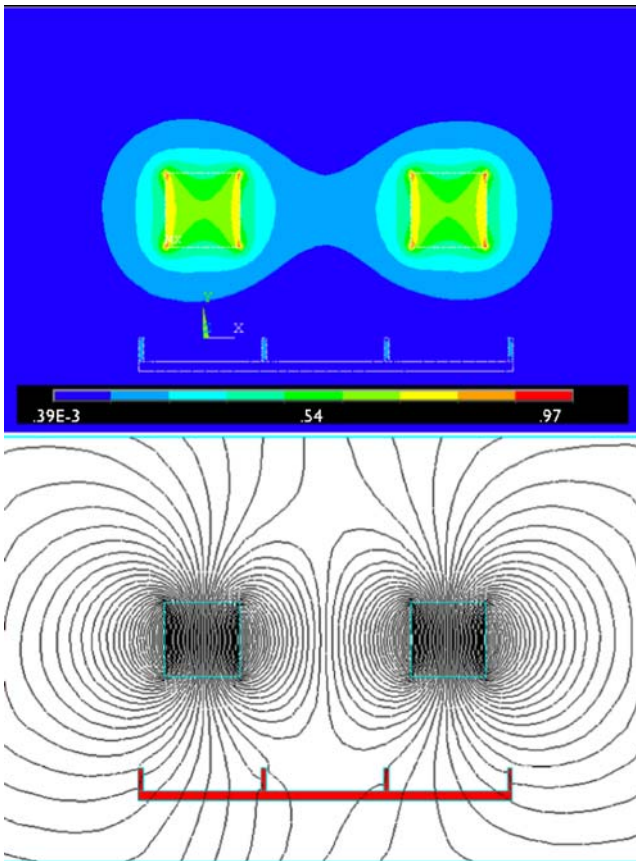


**Fig. 8** Results of the magnetic portion of the analysis. The top is the magnetic flux density in Teslas, and the bottom shows the field lines

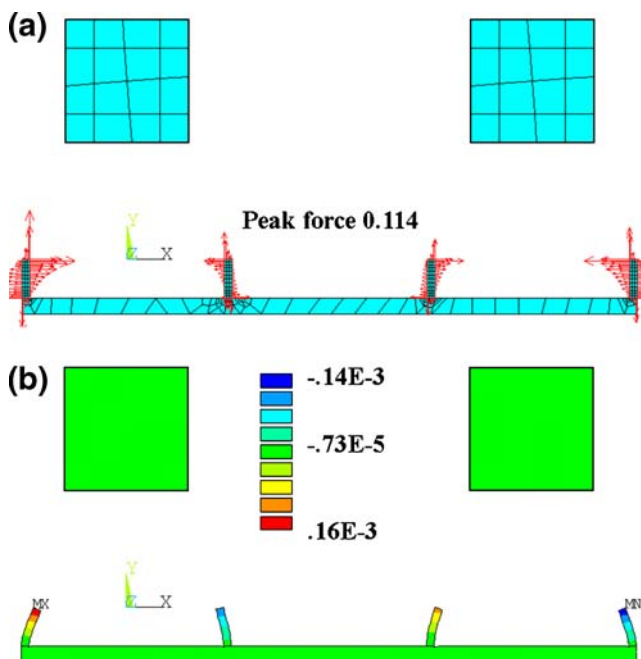


**Fig. 9** (a) Force in Newtons (from the Maxwell flags on the microflaps) resulting from the magnetic analysis. (b)  $U_x$  displacement results, in meters, resulting from the forces with constraints all around the air elements, the top of the magnets, and the bottom of the undeformed-PDMS region

manipulation has yet to be reported. Other studies have used magnetic microposts actuated by electromagnets instead of the permanent magnets used in this study. The microposts used in these studies were also made primarily of PDMS (Askeland 2002; Lemmon et al. 2005). While the micropost geometry in these studies is not the same as those used here (cylindrical instead of rectangular), the relative magnitudes of their displacements correspond to this paper’s findings. One study, however, shows that particles can also change their magnetic moment orientations with respect to the applied magnetic field (Sniadecki et al. 2007). The results of that study are not analogous to the current one because our permanent magnets do not have as concentrated of magnetic fields as the electromagnets used in by this group.

Other studies used microposts on a much smaller scale (10 times smaller on average) that focused primarily on cell isolation rather than on the isolation and straining of a group of cells (Miller 2001; Sniadecki et al. 2007). Still other studies have examined more closely the pure mechanical engineering aspect of this problem, obtaining

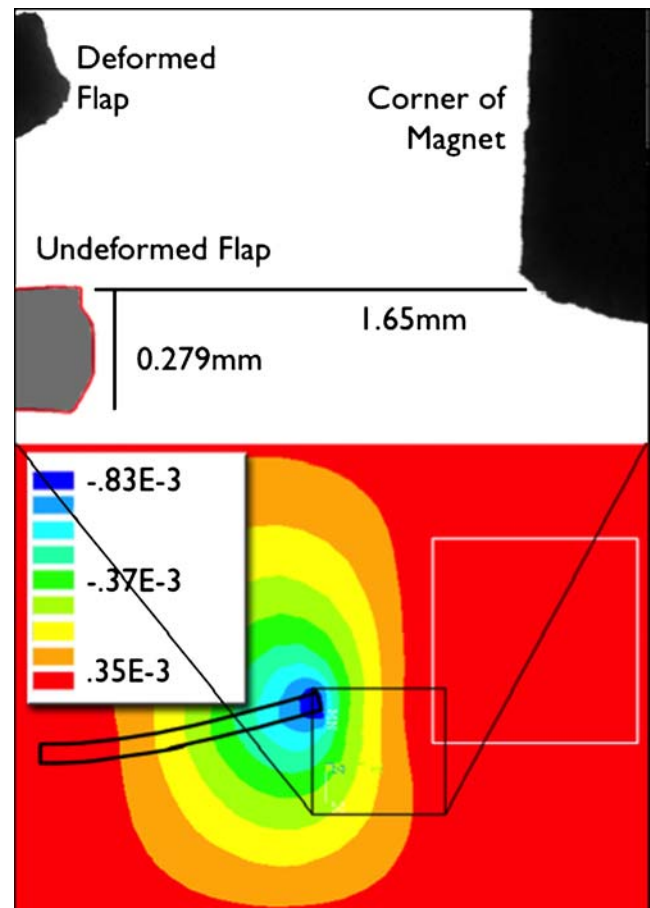


**Fig. 10** Top) Thresholded image of undeformed (grey) and deformed (black) microflap. Bottom) Finite element simulation of this displacement

results that follow the classical beam bending approach (for a prismatic beam) shown in Eq. 19 (Gere 599 2004).

$$M = EI \frac{d^2v}{dx^2} \quad (19)$$

When putting in the forces displayed in Fig. 7 one can use this equation and obtain the deflections displayed in Fig. 8. Some studies, however, considered the magnetic force to be a uniform or singular force, whereas the results here suggest the force decreases as  $r^2$ , which is what realistically occurs (Serway et al. 2000).

There are several limitations to the current study. While the model is accurate enough to predict a scaled up physical model, several additional concerns should be considered before fabricating the final MF arrangement design. The material properties of the PDMS will change when doped with iron-filings. Using the small density allows the elasticity to remain fairly unchanged, but benchtop mechanical testing will prove useful before creating a more complicated 3D model to mimic the final test fixture. Testing the permeability of the final cured product would also increase the model accuracy. Perhaps the most important limitation of the current study is the assumption that the MF deflection will result in a specific TEC strain (i.e., there is a one-to-one transmission between MF displacement and tissue strain). Current work in our laboratory is aimed at testing this assumption. Finally, it also stands to reason that the mechanical properties of the TEC itself, while not as stiff as PDMS, may also eventually influence MF displacement (Ashton et al. 2009).

The present study concluded that magnetically doped-PDMS magneto-structural characteristics can be simulated in a computational environment. Several key aspects in the design of the magnetic actuator have been identified. Such analysis will aid in microdevice development, and may eventually lead to systems capable of stimulating TECs in nonhomogenous and preferred directions at idealized length scales.

**Acknowledgements** The authors would like to especially thank Jennifer Watson. Partial funding for this work was provided by an NSF CAREER (0644570) award to JPVG.

## References

- M. Eastwood, V.C. Muderu, D.A. McGrouther, R.A. Brown, Effect of precise mechanical loading on fibroblast populated collagen lattices: morphological changes. *Cell Motil Cytoskeleton* **40**(1), 13–21 (1998)
- K. Kanda, T. Matsuda, Mechanical stress-induced orientation and ultrastructural change of smooth muscle cells cultured in three-dimensional collagen lattices. *Cell Transplant* **3**(6), 481–92 (1994)
- D. Seliktar, R.A. Black, R.P. Vito, R.M. Nerem, Dynamic mechanical conditioning of collagen-gel blood vessel constructs induces remodeling *in vitro*. *Ann Biomed Eng* **28**(4), 351–62 (2000)

- S.W. Liao, K. Hida, J.S. Park, S. Li, Mechanical regulation of matrix reorganization and phenotype of smooth muscle cells and mesenchymal stem cells in 3D matrix. *Conf Proc IEEE Eng Med Biol Soc* **7**, 5024–7 (2004)
- G.E. Wnek, G.L. Bowlin, *Encyclopedia of Biomaterials and Biomedical Engineering*. Vol. Tissue Engineering of Skeletal Muscle. Informa Health Care. (2008)
- N. L'Heureux, S. Paquet, R. Labbe, L. Germain, F.A. Auger, A completely biological tissue-engineered human blood vessel. *FASEB J* **12**(1), 47–56 (1998)
- J.A. McKee, S.S. Banik, M.J. Boyer, N.M. Hamad, J.H. Lawson, L.E. Niklason, C.M. Counter, Human arteries engineered *in vitro*. *EMBO Rep* **4**(6), 633–8 (2003)
- L.E. Niklason, J. Gao, W.M. Abbott, K.K. Hirschi, S. Houser, R. Marini, R. Langer, Functional arteries grown *in vitro*. *Science* **284**(5413), 489–93 (1999)
- D.H. Kim, P.K. Wong, J. Park, A. Levchenko, and Y. Sun, *Microengineered Platforms for Cell Mechanobiology*. *Annu Rev Biomed Eng*. (2009)
- D. Armani, *Re-configurable fluid circuits by PDMS elastomer micro-machining*. in *Twelfth IEEE International Conference on Micro Electrical Mechanical Systems*. (1999)
- K. Miller, How to test very soft biological tissues in extension? *J Biomech* **34**(5), 651–7 (2001)
- J.L. Tan, J. Tien, D.M. Pirone, D.S. Gray, K. Bhadriraju, C.S. Chen, Cells lying on a bed of microneedles: an approach to isolate mechanical force. *Proc Natl Acad Sci U S A* **100**(4), 1484–9 (2003)
- M. Khoo, C. Liu, Micro magnetic silicone elastomer membrane actuator. *Sensors and Actuators* **89**, 259–266 (2001)
- A. Kretschmer, R. Drake, M. Neidhoefer, M. Wilhelm, Quantification of composition and domain sizes of industrial poly(phthalamide)/poly(dimethylsiloxane) block copolymers using different 1H solid state NMR methods. *Solid State Nucl Magn Reson* **22**(2–3), 204–17 (2002)
- D. Sadler, T. Liakopoulos, J. Cropp, C. Ahn, T. Henderson, Prototype microvalve using a new magnetic microactuator. *SPIE Conference on Microfluidic Devices and Systems* **3515**, 3515–03 (1998)
- N.J. Sniadecki, A. Anguelouch, M.T. Yang, C.M. Lamb, Z. Liu, S.B. Kirschner, Y. Liu, D.H. Reich, C.S. Chen, Magnetic microposts as an approach to apply forces to living cells. *Proc Natl Acad Sci U S A* **104**(37), 14553–8 (2007)
- K&J Magnetics, I. *Neodymium Magnet Physical Properties*. Available from: <http://www.kjmagnetics.com/specs.asp> 2007
- J. Gere, *Mechanics of Materials*. Sixth Edition ed. Brooks/Cole. 599. (2004)
- A.E. Brown, *Rationale and summary of methods for determining ultrasonic properties of materials at Lawrence Livermore Laboratory*. (1995)
- X. Wang, M. Tillack, S.S. Harilal, *2-D Magnetic circuit analysis for a permanent magnet used in laser ablation plume expansion experiments* (University of California, La Jolla, 2003)
- ANSYS, I., *Theory Reference*. Canonsburg: ANSYS, Inc. (2006)
- D. Askeland, *The Science and Engineering of Materials*. Fourth Edition ed. Thomas-Engineering. (2002)
- C.A. Lemmon, N.J. Sniadecki, S.A. Ruiz, J.L. Tan, L.H. Romer, C.S. Chen, Shear force at the cell-matrix interface: enhanced analysis for microfabricated post array detectors. *Mech Chem Biosyst* **2** (1), 1–16 (2005)
- R. Serway, R. Beichner, J.W. Jewett, *Physics for Scientists*, 5th edn. (Saunders College Publishing, Orlando, 2000)
- J.H. Ashton, J.P. Vande Geest, B.R. Simon, D.G. Haskett, Compressive mechanical properties of the intraluminal thrombus in abdominal aortic aneurysms and fibrin-based thrombus mimics. *J Biomech* **42**(3), 197–201 (2009)